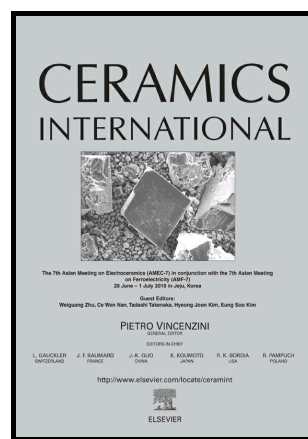# Author's Accepted Manuscript

Battery-like behavior of Ni-ceria based systems: synthesis, surface defects and electrochemical assessment

Allan J.M. Araújo, Vinícius D. Silva, Angel R.O. Sousa, João P.F. Grilo, Thiago A. Simões, Daniel A. Macedo, Rubens M. Nascimento, Carlos A. Paskocimas

This is a PDF file of an unedited manuscript that has been accepted for publication. As a service to our customers we are providing this early version of the manuscript. The manuscript will undergo copyediting, typesetting, and review of the resulting galley proof before it is published in its final citable form. Please note that during the production process errors may be discovered which could affect the content, and all legal disclaimers that apply to the journal pertain.

Battery-like behavior of Ni-ceria based systems: synthesis, surface defects and electrochemical assessment

Allan J. M. Araújo[a,*], Vinícius D. Silva[b], Angel R. O. Sousa[a], João P. F. Grilo[c]

Thiago A. Simões[b], Daniel A. Macedo[b,*], Rubens M. Nascimento[a], Carlos A. Paskocimas[a]

[a]Materials Science and Engineering Postgraduate Program, UFRN, 59078-970, Natal, Brazil

[b]Materials Science and Engineering Postgraduate Program, UFPB, 58051-900, João Pessoa, Brazil

[c]Department of Materials and Ceramic Engineering, University of Aveiro, 3810-193 Aveiro, Portugal

allanmenezes@ufrn.edu.br

damaced@pq.cnpq.br

[*]Corresponding author: Tel.: +55 83 32167860; fax: +55 83 32167906

ABSTRACT

NiO, CeO_2 and respective composites are extensively used in energy storage devices due to mostly their high electrochemical activity. However, the assessment of battery-like behavior of Ni-ceria based systems comprising (Ni or Gd)-doped ceria combined with NiO seems to be neglected in the literature. In this work, NiO and ceria-based solid solutions composite powders were obtained by a co-precipitation synthesis method. The structure and particle size of the calcined powders were investigated by X-ray diffractometry (XRD) and field emission scanning electron microscopy (FESEM), respectively. Oxidative states of composites were inspected by X-ray photoelectron spectroscopy (XPS). The electrochemical performance of powders was evaluated by cyclic voltammetry, galvanostatic charge-discharge and impedance spectroscopy. Refinement of the XRD patterns showed that powders have nanosized crystallites and mean size of particles within

20 – 70 nm were revealed by FESEM. The improved specific capacity of the NiO-CeO$_2$ electrode material (about 2.5 times higher than that of NiO-CGO at 5 mV s^{-1}) is due to an increase in Faradic reactions taken place on its surface with a higher fraction of defects (namely Ni^{3+}, Ce^{3+} and oxygen vacancies), as determined by XPS. The superior electrochemical performance of the NiO-CeO$_2$ electrode is also confirmed by electrochemical impedance spectroscopy.

Graphical Abstract:
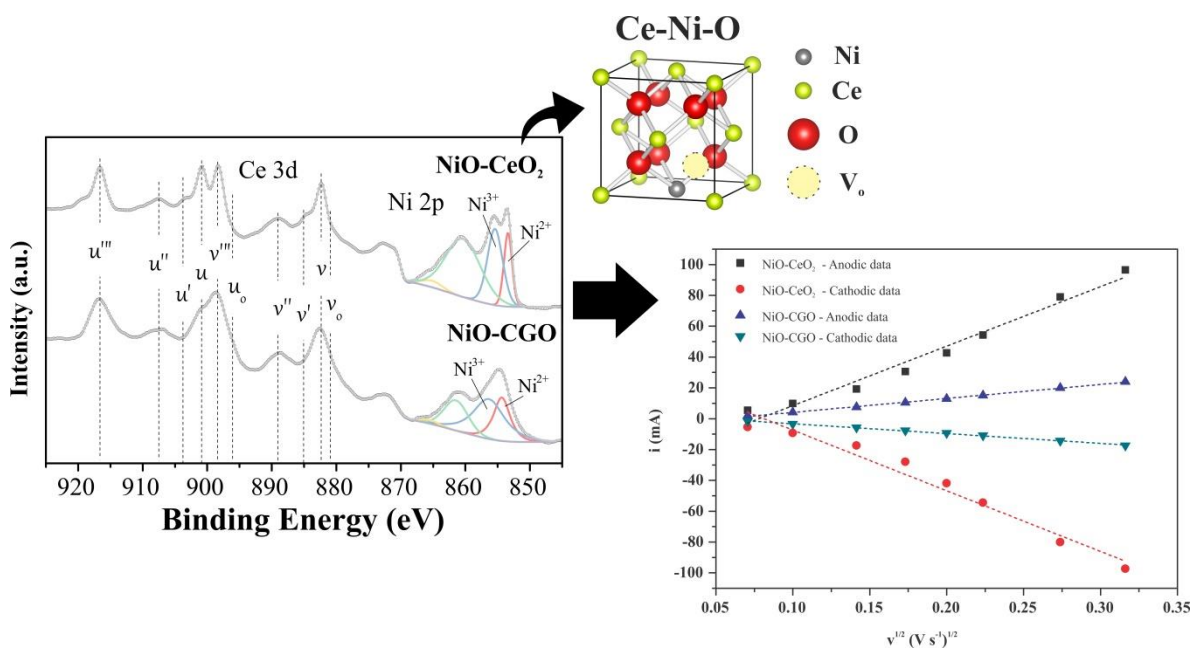
Keywords: Powder synthesis; NiO; CeO$_2$; doped ceria; battery-like electrodes.

1.   Introduction

Supercapacitors (also known as electrochemical capacitors) and batteries are promising electrochemical energy storage (EES) devices that have attracted significant attention due to the increasing demand for electrical energy supply. Unlike batteries, supercapacitors present higher power density, faster charge-discharge and longer cycle life. However, they have lower energy density than Li-ion batteries commonly used in

domestics electronics [1–4]. Batteries are considered one of the most important and efficient energy storage devices due mostly to advances in their higher specific capacity and long cycling life [5]. Among other characteristics, the electrodes play a significant role in battery performance. In the electrodes, Faradic redox reactions responsible to the charge and discharge of the battery take place, therefore, transition metal oxides (TMOs) are preferably used to manufacturing these components [6–9]. TMOs ions can present fast and reversible surface redox reactions properties with OH^-, which is the most desirable scenario for enhanced performance of EES devices charge storage [10–13]. Additionally, TMOs as RuO_2, NiO, MnO_2, Co_3O_4, and misfit-layered $Ca_3Co_4O_9$ compounds are known to have high electronic conductivity and electrochemical performances [5,14–21]. Research efforts are currently focused on producing low-cost electrodes with high theoretical capacities. Among promising electrode materials, NiO exhibits enhanced cycling properties and fast charge transfer when compared to others low-cost metal oxides with low capacity and limited power density [22–24]. In the current context, the discussion regarding capacitors and batteries, in which the electrochemical behavior is prevailingly characteristic of battery-like materials rather than pseudocapacitive materials seem to be unclear observing the literature [10,11,25,26]. Independently, the materials selection for storage properties devices must take into consideration the close relation between specific surface of metal oxides particles and electrochemical activity properties.

CeO_2 (ceria) is also extensively studied because of its interesting redox properties (fast oxidation state change of Ce^{4+} to Ce^{3+} in a certain range of temperature and pressure of oxygen), high oxygen storage capacity (ability to store and release oxygen depending on the reaction condition), hydrophilic behavior (increasing the surface active sites), and environmentally friendly characteristics [27–29]. It is well known that the redox properties of ceria can be considerably enhanced if additional elements are introduced into its lattice [30–32]. Density functional theory (DFT) studies of ceria doped with divalent Ni reported the potential for this dopant (lowering the formation energy of oxygen vacancies and favoring the formation of Ce^{3+} from Ce^{4+}) to be used in ceria-based materials for catalysis or solid oxide fuel cells [33,34]. Despite NiO and CeO_2 materials have been extensively studied separately as electrodes for energy storage applications [28,35–37], the electrochemical performance of the NiO-CeO_2 composite was punctually studied [38] and

3

no report was found for (Ni or Gd)-doped ceria/NiO composites. Following the trend of $NiO-Ce_{0.9}Gd_{0.1}O_{1.95}$ (NiO-CGO) applications as precursors of energy conversion devices [39–42], the present work is focused on evaluating the effects of Ni or Gd-doped ceria on battery-like behavior of Ni-ceria based systems. The electrochemical assessment was carried out by cyclic voltammetry, galvanostatic charge-discharge and electrochemical impedance spectroscopy at room temperature in an alkaline (3 M KOH) solution. Considering that electrochemical reactions are favored if the formation of oxygen vacancies and Ce^{3+} is facilitated [43], type and concentration of surface defects were analyzed by X-ray Photoelectron Spectroscopy (XPS).

2.   Experimental

NiO-CeO_2 (more precisely NiO + Ce-Ni-O solid solution) and $NiO-Ce_{0.9}Gd_{0.1}O_{1.95}$ (NiO-CGO) composite powders, with 50 wt.% NiO, were synthesized by a co-precipitation method using $Ce(NO_3)_3.6H_2O$ (Sigma-Aldrich, 99.0%) and $Ni(NO_3)_2.6H_2O$ (Sigma-Aldrich, $\geq$ 97.0%) as starting materials. In a typical co-precipitation procedure (Fig. 1), appropriate amounts of Ce and Ni nitrates were dissolved in an alcoholic solution and continuously stirred at room temperature to form a homogeneous solution. The concentrations of the stock solutions were 0.232 and 0.238 mol L^{-1} for Ce^{4+} and Ni^{2+}, respectively. NH_4OH solution (Merck, 27% of ammonia) was used as a precipitating agent. 20 wt.% above the required amount of the NH_4OH solution (27%) was used to precipitate metal cations into the mixed gel. The precipitation occurred at a pH value of 9. Traces of NH_4OH were further removed by vacuum centrifugation. The gel was dried for 2 h at 100 °C, resulting in a finely powdered xerogel that was calcined in air at 800 ℃ for 2 h to obtain the NiO-CeO_2 composite. For the synthesis of the composite with Gd-doped ceria (NiO-$Ce_{0.9}Gd_{0.1}O_{1.95}$), $Gd(NO_3)_3.6H_2O$ (Sigma-Aldrich, 99.9%) was also used, following the same experimental procedure described above. The concentrations were 0.104, 0.009 and 0.134 mol L^{-1} for Ce^{4+}, Gd^{3+} and Ni^{2+}, respectively. CeO_2 powder was also synthesized and further calcined at 800 °C for 2 h to assess the solubility of Ni cations into the ceria lattice.

4

Phase identification of the synthesized and calcined powders was performed at room temperature by X-ray diffractometry (XRD) in the range of 20-80º (2θ), 0.02º step sizes and 1º min^{-1} scanning speed, operating with a voltage 40 kV and current of 30 mA using Cu Kα radiation (Shimadzu, model XRD 7000). Rietveld refinement of the diffraction data was performed using MAUD software (Materials Analysis Using Diffraction). The crystallite sizes were estimated using a Voigt methodology proposed by Keijser et al. [44]. The chemical states at the surfaces were studied using X-ray Photoelectron Spectroscopy (XPS). The analyses were carried out in an Ultra High Vacuum (UHV) system with a base pressure of $2x10^{-10}$ mbar located at TEMA, University of Aveiro (Portugal), using a SPECS Phoibos 150 spectrometer with a high intensity monochromatic Al Kα X-ray source (1486.6 eV). High-resolution spectra were recorded at normal emission take-off angle and with a pass-energy of 20 eV, which provides an overall instrumental peak broadening of 0.5 eV. The binding energy was referenced to C 1s line at 285 eV for calibration. Using CasaXPS fitting software, the height, area and position of the peaks were determined to ally the separation of measured XPS spectra. Powder morphological inspection was carried out using field-emission scanning electron microscopy (FESEM, Carl Zeiss, Supra 35-VP Model) equipped with a Bruker EDS detector (XFlash 410-M). The specific surface area of calcined powders was determined by N_2 adsorption at -196 ºC in a BELSORP-mini II (BEL Japan Inc., Japan) analyzer using BET (Brunauer, Emmett and Teller) method. Prior to analysis, powders were degassed under vacuum at 300 ºC for 3 h.

Cyclic voltammetry (CV), galvanostatic charge-discharge (GCD) and electrochemical impedance spectroscopy (EIS) were used to assess the performance of the electrodes. All electrochemical studies were performed using a PGSTAT204 with FRA32M module (Metrohm Autolab) in a three-electrode setup in 3 M KOH in deionized water. A platinum plate and Ag/AgCl were used as counter and reference electrodes, respectively. To prepare the working electrode, 80 wt.% active material, 10 wt.% carbon black and 10 wt.% polytetrafluoroethylene (PTFE) (60 wt.% PTFE dispersion in H_2O) were dispersed in isopropyl alcohol and sonicated for 30 min. Then, inks containing each composite powder

were drop-casted on Ni foams (1×1 cm^2), previously cleaned by sonicated during 10 min in 2 M HCl, acetone, and deionized water, respectively; for the removal of the oxide layer. Finally, working electrodes were heated at 100 °C for 12 h in a vacuum oven to remove residual solvent, and then pressed at 1 ton for 30 s. The mass loading of the electrode material on Ni foam was about 5 mg cm^{-2}. CV analysis was performed between 0-0.5 V vs. Ag/AgCl at scan rates ranging from 5 to 100 mV s^{-1}. In the CV tests, specific capacities values at different scan rates were calculated by Eq. 1 [45].

$$Q_s = \frac{\int IdV}{2mv} \tag{1}$$

where the numerator value can be estimated from the CV curve area and the denominator is double the product of the weight of the active material in each electrode (m) and the scan rate (v). For comparison, a blank Ni foam was also studied under the same conditions. The GCD test was conducted in a potential window of 0-0.45 V at a specific current of 0.5 A g^{-1}. The specific capacity was then calculated using Eq. 2 [45].

$$Q_s = \frac{I\Delta t}{m} \tag{2}$$

where m, Δt and I are weight of the active material (g), discharge time (s) and discharge current, respectively. Electrochemical impedance spectroscopy (EIS) was performed when the working electrode was biased at a constant potential of 0.32 V vs. Ag/AgCl in the frequency range 0.01-100 kHz using a voltage amplitude of 5 mV.

3.   Results and Discussion

X-ray diffraction patterns (XRD) and refinement fitting of calcined powders are shown in Fig. 2. The obtained low values of goodness-of-fit ($\chi^2 = R_{wp}/R_{exp}$), shown in Fig. 2a, indicate excellent agreement between data and refined models. The expected crystalline phases were formed after calcination, demonstrating that precursor powders were readily oxidized to NiO-CeO$_2$ and NiO-CGO nanoparticles. Diffraction peaks were indexed using the space group Fm$\bar{3}$m (225) of the sodium chloride-type crystal structure of NiO (ICSD collection code: 24018), fluorite-type cubic structure of CeO$_2$ (ICSD collection code:
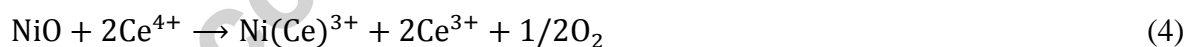
6

88759) and fluorite-type cubic structure of $Ce_{0.9}Gd_{0.1}O_{1.95}$ (ICSD collection code: 28795), as shown in Fig. 2b. For the prepared composites, peaks of the two phases (CeO_2/CGO and NiO) emerged separately without the existence of an unexpected crystalline phase. NiO-CeO_2 and NiO-CGO showed prominent diffraction peaks at 37.3º, 43.3º, 62.9º, 75.4º, and 79.4º corresponding to (111), (200), (220), (311), and (222) crystal planes of the NiO phase. The peaks of the CeO_2/$Ce_{0.9}Gd_{0.1}O_{1.95}$ phase were observed at 28.6º, 33.1º, 47.5º, 56.4º, 59.1º, 69.5º, 76.7º, and 79.1º, corresponding to (111), (200), (220), (311), (222), (400), (331), and (420) crystal planes. It is worth mentioning that the CeO_2 structure may be modified by Ni^{2+} substitution, which further gives rise to a Ce-Ni-O solid solution or even a mixture NiO + Ce-Ni-O whether the nickel content surpasses its solubility limit in the lattice of ceria. In fact, a solubility limit of about 15 at% Ni^{2+} in CeO_2 crystals was recently reported by Mahammadunnisa et al. [32]. In the case of the NiO-CGO composite, the diffusion of Ni^{2+} in the Gd-doped ceria (CGO) lattice may be slower than that of Gd cations, thus restricting the growth of the CGO phase.

Structural parameters of powders estimated by Rietveld refinement are shown in Table 1. A weight ratio ca. 1:1 (1.00 and 1.20% difference for NiO-CGO and NiO-CeO_2, respectively) of NiO and CeO_2/CGO phases demonstrate an excellent control of phase composition achieved through the proposed synthesis procedure. The obtained lattice parameters, a = 4.1795 Å, a = 5.410 Å and a = 5.418 Å, for NiO, CeO_2 and CGO phases, respectively, are in agreement with their respective ICSD files and literature values for NiO-$Ce_{1-x}Gd_xO_{2-\delta}$ (x = 0 or 0.1) composites [40,46,47]. NiO lattice parameters in the current work are close to that of NiO standard (ICSD collection code: 24018). The Gd^{3+} insertion promotes a slightly change into ceria fluorite structure when compared to undoped ceria. Such phenomenon is well reported and can be attributed to the replacement of Ce^{4+} for Gd^{3+} with ionic radii of 0.097 and 0.105 nm, respectively [48]. Doping cubic fluorite-type structure of ceria with Gd^{3+} ions rises one oxygen vacancy for every two Gd^{3+} ions in order to maintain the crystal electrical neutrality. The formation of gadolinia-doped ceria may be represented by the following Kröger-Vink notation (Eq. 3):

7

$$Gd_2O_3 + 2Ce_{Ce}^x + O_O^x \rightarrow 2Gd_{Ce}' + V_O^{\bullet\bullet} + 2CeO_2 \tag{3}$$

Where, Gd_{Ce}' indicates one Ce^{4+} site occupied by Gd^{3+} ion and $V_O^{\bullet\bullet}$ represents the oxygen vacancy [49]. The defect structure of the Gd-doped ceria of the composition $Ce_{0.9}Gd_{0.1}O_{1.95}$ is shown in Fig. 2b. The calculated crystallite size of NiO is slightly larger than those of CeO_2/CGO (4-8 nm difference), in accordance with literature reports [39,40,50,51]. It is expected since the activation energy for Ni diffusion in NiO (184–255 kJ/mol) is energetically more demanding than that for Ce diffusion in CeO_2 (498 kJ/mol) [52,53]. Any solubility between NiO and CeO_2 should decrease the cubic CeO_2 lattice parameter due to the smaller ionic radius of Ni^{+2} (0.72 Å) when compared to Ce^{+4} (0.97 Å). In fact, the calculated (by refinement over raw XRD pattern, not shown) lattice parameter a = 5.412 Å for the synthesized single-phase CeO_2 powder suggests that one possible Ni dissolution in the CeO_2 structure, originating a mixed (Ce-Ni-O, a = 5.410 Å) oxide, seems to be likely after calcination at 800 °C in air. This result is in good agreement with the lattice parameter decrease through Ni doping reported by Kumar et al. [54]. One may suppose that the presence of Ce^{3+} ions could prohibit some lattice contraction due to its larger ionic radius (1.07 Å) compared to Ce^{+4}. In addition, the replacement of Ce^{4+} for Ni^{2+} would be also expected to create extrinsic oxygen vacancies, known to expand the lattice parameter of fluorite-type structure [55]. Doping cubic fluorite-type structure of ceria with Ni^{2+} ions rises a single oxygen vacancy for each Ni^{2+} ion in order to maintain the crystal electrical neutrality. The formation of Ce-Ni-O solid solutions may be represented by the following reactions (Eqs. 4-6) [56]:

$$NiO + 2Ce^{4+} \rightarrow Ni(Ce)^{3+} + 2Ce^{3+} + 1/2O_2 \tag{4}$$

$$NiO + 2Ce^{4+} \rightarrow 2Ni_\Delta + 2Ce^{3+} + 1/2O_2 \tag{5}$$

$$NiO + Ce^{4+} \rightarrow 2Ni(Ce^{4+}) + Ce^{4+} + A.V. \tag{6}$$

Where Ni_Δ are Ni^{2+} ions retained in the interstitial positions; $Ni(Ce^{4+})$ and $Ni(Ce^{3+})$ are Ni^{2+} ions located in the positions of the host Ce^{4+} ions in the CeO_2 lattice and A.V. is anionic (oxygen) vacancy. Oxygen vacancy formation is connected with the change in oxidation state of cerium from oxidized Ce^{4+} to reduced Ce^{3+}. The substitutional solid solution is predicted (with basis in Ab initio thermodynamics) to be more stable than the interstitial

one by more than 2.4 eV [57]. A typical scheme of the crystal structure of the Ce-Ni-O solid solution in which Ni^{2+} ions occupy substitutional sites is shown in Fig. 2b.

Fig. 3 shows microstructure images of powders at low and high-magnification, including elementary maps of both composites. Fig. 3a depicts typical low magnification FESEM images of powders with high-density morphologies. The micrographs with high-magnification (Fig. 3b) clearly indicate the presence of aggregated nanoparticles of different sizes and shapes. The large particle aggregation is due to the presence of nanosized crystals with large surface energy. The particle size (Fig. 3c) of the $NiO-CeO_2$ powder (23 ± 3 nm) is in agreement with the crystallite size retrieved from the XRD patterns (Table 1). On the other hand, the NiO-CGO powder is composed of nanoparticles with a size close to 70 nm, almost twice the values estimated by refined crystallite sizes (Table 1). EDS mapping of $NiO-CeO_2$ (Fig. 3d) and NiO-CGO (Fig. 3e) composites shows a homogeneous distribution of Ni, Ce and Gd elements at the nanoscale.

The surface areas of the calcined powders were investigated using nitrogen adsorption analyses. As shown in Fig. 4, the steep increase in the amount of N_2 adsorption for $NiO-CeO_2$ was larger than NiO-CGO, with a sudden increment in the high-pressure region which is characteristic of type II isotherm (according to IUPAC classification). BET surface area and total pore volume ($P/P_0 = 0.973$) of $NiO-CeO_2$ (6.06 m^2 g^{-1} and 0.017 cm^3 g^{-1}) were slightly higher than those of NiO-CGO (5.04 m^2 g^{-1} and 0.007 cm^3 g^{-1}). The low surface area of both composite powders impairs the electrolyte (KOH solution) access to the NiO and CeO_2/CGO electroactive sites where reversible surface redox (Faradic) reactions occur. Taking that into account, the surface areas of these materials should not have any influence on their electrochemical performances.

The deconvoluted XPS spectra of $NiO-CeO_2$ and NiO-CGO powders are shown in Fig. 5. Core level of high-resolution spectra of the Ni 2p and Ce 3d regions were deconvoluted to reveal Ni and Ce oxidation states. The overview spectra (Fig. 5a) show

9

several electronic structures that can be attributed to photoelectrons excited from the Ce (3d), Ni (2p), O (1s), and C (1s) core energy levels. Peaks originating from Ni LMM and Ce MNN Auger processes are also present. Furthermore, NiO-CGO shows peaks attributed to Gd (3d), confirming the presence of Gd-doped ceria. The Ce ions in the Ce^{4+} state were assigned to Ce $3d_{5/2}$ (v, $v^{//}$ and $v^{///}$) and Ce $3d_{3/2}$ (u, $u^{//}$ and $u^{///}$) and those in the Ce^{3+} state were assigned to Ce $3d_{5/2}$ (v_0 and $v^{/}$) and Ce $3d_{3/2}$ (u_0 and $u^{/}$) [58,59], as shown in Fig. 5b. NiO-CeO$_2$ presents 25% of Ce^{3+} and 75% of Ce^{4+}, whereas NiO-CGO presents 21% of Ce^{3+} and 79% of Ce^{4+}. The higher Ce^{3+} content in NiO-CeO$_2$ may be due to the reduction of ceria enhanced by the synergic effect of nickel [60]. Due to this, NiO-CeO$_2$ triggered the creation of oxygen vacancies which is further confirmed via deconvolution of O 1s XPS spectra. Moreover, NiO is a p-type oxide, where the mobile species are cations. They diffuse through lattice defect sites such as vacancies and/or grain boundaries to the oxide/interface where they react with O$_2$. For NiO, defect formation involves the creation of a Ni^{2+} vacancy at the oxide/interface and, to balance charge, two neighboring Ni^{2+} atoms each lose an electron forming two Ni^{3+} (electron holes) [61]. XPS estimated Ni^{2+}/Ni^{3+} ratio was 0.5 and 0.6 for NiO-CeO$_2$ and NiO-CGO, respectively. The O1s scan (Fig. 5c) shows the spectra with three main peaks observed: 529.9 eV (O$_L$), 532.2 eV (O$_V$) and 535.8 eV (O$_H$) [32,62]. The first peak (O$_L$) is oxygen in lattice often associated with metal-oxygen bonds. The second peak (O$_V$) is attributed to defective sites with low oxygen coordination (vacancies). One can correlate O$_L$ and O$_V$ intensity ratio to oxygen vacancies. NiO-CeO$_2$ shows a Ov/O$_L$ ratio of 0.87, against 0.02 for NiO-CGO. The third peak (O$_H$) is associated with hydroxyl groups/organic species/H$_2$O absorption. XPS analyses suggested that NiO-CeO$_2$ exhibited maximum surface defects in the form of Ce^{3+}, Ni^{3+} and oxygen vacancies which are expected to boost the electrochemical performance.

Cyclic voltammetry (CV) was performed to assess the effect of (Ni or Gd)-doping on the electrochemical performance of composites deposited onto Ni foams. Figs. 6a, b show CV curves of NiO-CeO$_2$ and NiO-CGO electrodes at various scan rates (5-100 mV s$^-$

[1]). Typical CV responses, showing clearly separated oxidative and reductive peaks, are characteristics of battery-like behavior [25]. The well-resolved redox peaks can be observed for both samples, within the measured potential window, indicating the battery-like behavior can be attributed to fast and reversible Faradic redox reactions of mixed Ni^{2+}/Ni^{3+} and Ce^{3+}/Ce^{4+} couples highlighted by XPS, together with contributions of oxygen vacancies. The broad anodic peaks (oxidation) can be seen at 0.33 and 0.32 V for NiO-CeO_2 and NiO-CGO, respectively, and the cathodic peaks (reduction) at 0.19 and 0.22 V for NiO-CeO_2 and NiO-CGO, respectively. As the scan rate increases, the cathodic peak shifted towards negative potentials while the anodic peak shifted towards positive potentials, which is ascribed due to the electrode polarization effect. The prominent and broad peaks in the NiO-CeO_2 electrode confirm the contribution of the redox behavior of the ceria phase (Ce^{3+}/Ce^{4+}) in the surface redox reaction. However, redox peaks of Ni^{2+}/Ni^{3+} and Ce^{3+}/Ce^{4+} were not discernible in the CV curves. Such characteristic is probably due to the match of potential range of the reversible valence change between Ce^{3+}/Ce^{4+} and Ni^{2+}/Ni^{3+} [38]. These processes can be explained by the following reversible reactions (Eqs. 7, 8) [29,63]:

$$NiO + OH^- \leftrightarrow NiOOH + e^- \tag{7}$$

$$Ce^{IV}O_2 + K^+ + e^- \leftrightarrow Ce^{III}O \cdot OK \tag{8}$$

The anodic and cathodic peak currents of the CV curves grow with the increasing scan rate. Besides, curves width remains unaltered over the entire scan rate range. It reveals a good kinetics reversibility of the OH^- ions, improved mass transport and fast electronic/ionic transport rates. That demonstrates a good stability of the alkaline electrolyte with the electrode material for battery application. Fig. 6c shows the CV curves of NiO-CeO_2, NiO-CGO electrodes and a blank Ni foam (for sake of comparison) at a constant scan rate of 100 mV s^{-1}. It is possible to note that the area under the CV curve for the Ni foam is very small compared to those of Ni-ceria based electrodes, which shows that its contribution to the capacity is insignificant. Analyzing the curves of the electrodes, it can be seen that the CV curve of NiO-CGO is much smaller than that of NiO-CeO_2. The increased particle size of the NiO-CGO electrode (70 nm vs. 23 nm for NiO-CeO_2) suggests a size-dependent electrochemical performance enhanced with decreasing particles size, as reported in previous works [64,65]. Indeed, peak currents recorded in cyclic

voltammetry of the $NiO-CeO_2$ electrode are higher than those of NiO-CGO (Fig. 6c), indicating particles with smaller size have higher electrochemical activity. The CV data for the composite electrodes at different scan rates (Figs. 6a, b) were used to understand the contribution of diffusion-controlled processes. The plots of both anodic and cathodic scans are near-linear, for the two composites, with the coefficient of determination in the range of 96 to 99% (Fig. 6d). The slopes (b = $i_p/v^{1/2}$, where b is the slope, i_p is the peak current and v is the scan rate) of $NiO-CeO_2$ and NiO-CGO electrodes are 385.84 and 90.50 for anodic currents and -393.58 and -63.66 for cathodic currents, respectively, which determine diffusion rates with surface redox reactions taking place in charge storage processes [66]. Therefore, the rates of anodic/cathodic reactions on the surface of $NiO-CeO_2$ composite are very faster than that of the chemical reactions in NiO-CGO. These results confirm that the Faradic reactions occurring on the surface increase with increasing the concentration of surface defects. The specific capacities for each composite were then calculated from their voltammetric data at the different scan rates used, as shown in Fig. 6e. It is possible to observe that specific capacities increase with decreasing scan rate because higher fractions of OH^- involved in the reversible surface redox reactions (Eqs. 7 and 8) have more favorable conditions to access CeO_2/CGO and NiO particles. At a low scan rate, there is much time for the diffusion of ions through the electrode materials. As the scan rate increases, the diffusion of ions becomes limited, resulting in a less diffusive capacity [67]. In summary, CV tests demonstrated the electrochemical activity of the $NiO-CeO_2$ electrode surpasses that of the NiO-CGO, as predicted by the defect analysis done by XPS.

Fig. 7 shows the galvanostatic charge-discharge (GCD) curve for the $NiO-CeO_2$ composite (the best one in the CV tests) at a constant specific current of 0.5 A g^{-1}. The charging step shows a first linear stage corresponding to the oxidation of NiO (Ni^{2+}) to NiOOH (Ni^{3+}) and Faradic redox conversion of $Ce^{3+} \leftrightarrow Ce^{+4}$, and a second stage attributed to the charging process itself. The discharging curve (clearly non-linear) indicates potential plateaus related to Faradic reactions, confirming a battery-like behavior [4,25]. It can also be observed that charge and discharge times are quite similar (30.5 and 27.7 s, respectively), indicating a good coulombic efficiency [68]. From the GCD curve, the

electrode has a specific capacity of 14 C g^{-1} (estimated by Eq. 2), in good agreement with the value retrieved from the cyclic voltammetry at 5 mV s^{-1}. In addition to the characteristic Ce^{+4}/Ce^{+3} redox couple contribution, the hydrophilic nature of the CeO_2 is expected to increase the number of active surface sites [27,38]. Importantly, the observation of mixed Ni^{2+}/Ni^{3+} redox couple (Fig. 5b), with a slightly higher fraction of Ni^{3+} in the $NiO-CeO_2$ material, is expected to be a potentially useful factor for its enhanced electrocatalytic rates [69].

Impedance spectroscopy analyses were performed to understand the electrochemical behavior of $NiO-CeO_2$ and NiO-CGO electrodes during the charge storage process. Those results are shown as Nyquist plots in Fig. 8. The values of ESR (Equivalent Series Resistance – intercept at the real part in the high-frequency region) were 0.23 and 0.33 Ω for $NiO-CeO_2$ and NiO-CGO, respectively, showing a lower conductivity of the NiO-CGO composite during redox processes [70]. No semicircle was verified in the high-frequency region, suggesting fast charge transfer at the electrolyte/electrode interface [71]. In the low-frequency region, the slope of the straight-line is associated with a mass transfer resistance (Warburg impedance) during diffusion of the redox species [72]. The higher slope for the $NiO-CeO_2$ electrode manifests a faster diffusion of ions from the electrolyte [72,73].

4.   Conclusions

A co-precipitation synthesis method was successfully employed to prepare Ni-ceria based systems as battery-like materials. Electrodes made of these nanosized (double phase) particles were electrochemically evaluated by cyclic voltammetry, galvanostatic charge-discharge and impedance spectroscopy in alkaline (3 M KOH) solution. The $NiO-CeO_2$ electrode exhibited better electrochemical behavior with improved specific capacity (about 2.5 times higher than that of NiO-CGO at 5 mV s^{-1}) and smaller ESR (0.23 Ω vs. 0.33 Ω) than the $NiO-Ce_{0.9}Gd_{0.1}O_{1.95}$ electrode. The superior electrochemical performance of $NiO-CeO_2$ is ascribed due to an increased concentration of defects (Ni^{3+}, Ce^{3+} and oxygen vacancies) used to boost Faradic surface redox reactions.

Acknowledgements

References

[1]   S. Bose, T. Kuila, A.K. Mishra, R. Rajasekar, N.H. Kim, J.H. Lee, Carbon-based nanostructured materials and their composites as supercapacitor electrodes, J. Mater. Chem. 22 (2012) 767–784. doi:10.1039/C1JM14468E.

[2]   G. Wang, L. Zhang, J. Zhang, A review of electrode materials for electrochemical supercapacitors, Chem. Soc. Rev. 41 (2012) 797–828. doi:10.1039/C1CS15060J.

[3]   M. Vangari, T. Pryor, L. Jiang, Supercapacitors: Review of Materials and Fabrication Methods, J. Energy Eng. 139 (2012) 72–79. doi:10.1061/(ASCE)EY.1943-7897.0000102.

[4]   Y. Zhang, H. Feng, X. Wu, L. Wang, A. Zhang, T. Xia, H. Dong, X. Li, L. Zhang, Progress of electrochemical capacitor electrode materials: A review, Int. J. Hydrogen Energy. 34 (2009) 4889–4899. doi:10.1016/j.ijhydene.2009.04.005.

[5]   M. Sharma, S. Sundriyal, A.K. Panwar, A. Gaur, Facile synthesis and electrochemical performance of Mg-substituted $Ni_{1-x}Mg_xCo_2O_4$ mesoporous nanoflakes for energy storage applications, Electrochim. Acta. 294 (2019) 53–59. doi:10.1016/j.electacta.2018.10.085.

[6]   R. Li, Y. Wang, C. Zhou, C. Wang, X. Ba, Y. Li, X. Huang, J. Liu, Carbon-Stabilized High-Capacity Ferroferric Oxide Nanorod Array for Flexible Solid-State Alkaline Battery-Supercapacitor Hybrid Device with High Environmental Suitability, Adv. Funct. Mater. 25 (2015) 5384–5394. doi:10.1002/adfm.201502265.

[7]   X. Yu, B. Lu, Z. Xu, Super long-life supercapacitors based on the construction of nanohoneycomb-like strongly coupled $CoMoO_4$-3D graphene hybrid electrodes, Adv. Mater. 26 (2014) 1044–1051. doi:10.1002/adma.201304148.

[8]   S. Vijayakumar, S. Nagamuthu, K.S. Ryu, $CuCo_2O_4$ flowers/Ni-foam architecture as a battery type positive electrode for high performance hybrid supercapacitor applications, Electrochim. Acta. 238 (2017) 99–106. doi:10.1016/j.electacta.2017.03.178.

[9]   Z. Lin, E. Goikolea, A. Balducci, K. Naoi, P.L. Taberna, M. Salanne, G. Yushin, P. Simon, Materials for supercapacitors: When Li-ion battery power is not enough, Mater. Today. xxx (2018) 1–18. doi:10.1016/j.mattod.2018.01.035.

[10]   P. Simon, Y. Gogotsi, B. Dunn, Where Do Batteries End and Supercapacitors Begin?, Mater. Sci. 343 (2014) 1210–1211. doi:10.1126/science.1249625.

[11]   T. Brousse, D. Belanger, J.W. Long, To Be or Not To Be Pseudocapacitive?, J. Electrochem. Soc. 162 (2015) A5185–A5189. doi:10.1149/2.0201505jes.

[12]   H.C. Chen, Y. Qin, H. Cao, X. Song, C. Huang, H. Feng, X.S. Zhao, Synthesis of amorphous nickel–cobalt–manganese hydroxides for supercapacitor-battery hybrid energy storage system, Energy Storage Mater. (2018) 0–1. doi:10.1016/j.ensm.2018.07.018.

[13]   D.P. Dubal, O. Ayyad, V. Ruiz, P. Gómez-Romero, Hybrid energy storage: The merging of battery and supercapacitor chemistries, Chem. Soc. Rev. 44 (2015) 1777–1790. doi:10.1039/c4cs00266k.

[14]   P. Wang, Y. Xu, H. Liu, Y. Chen, J. Yang, Q. Tan, Carbon/carbon nanotube-supported RuO_2 nanoparticles with a hollow interior as excellent electrode materials for supercapacitors, Nano Energy. 15 (2015) 116–124. doi:10.1016/j.nanoen.2015.04.006.

[15]   G. Cai, X. Wang, M. Cui, P. Darmawan, J. Wang, A.L.S. Eh, P.S. Lee, Electrochromo-supercapacitor based on direct growth of NiO nanoparticles, Nano Energy. 12 (2015) 258–267. doi:10.1016/j.nanoen.2014.12.031.

[16]   P. Wang, Y.-J. Zhao, L.-X. Wen, J.-F. Chen, Z.-G. Lei, Ultrasound−Microwave-Assisted Synthesis of MnO_2 Supercapacitor Electrode Materials, Ind. Eng. Chem. Res. 53 (2014) 20116–20123. doi:10.1021/ie5025485.

[17]   S. Abouali, M. Akbari Garakani, B. Zhang, Z.-L. Xu, E. Kamali Heidari, J. Huang, J. Huang, J.-K. Kim, Electrospun Carbon Nanofibers with in Situ Encapsulated Co_3O_4

Nanoparticles as Electrodes for High-Performance Supercapacitors, ACS Appl. Mater. Interfaces. 7 (2015) 13503–13511. doi:10.1021/acsami.5b02787.

[18]   V.D. Silva, T.A. Simões, F.J.A. Loureiro, D.P. Fagg, E.S. Medeiros, D.A. Macedo, Electrochemical assessment of $Ca_3Co_4O_9$ nanofibres obtained by Solution Blow Spinning, Mater. Lett. 221 (2018) 81–84. doi:10.1016/j.matlet.2018.03.088.

[19]   N. Bagheria, A. Aghaei, N. Vlachopoulos, M. Skunik-Nuckowska, P.J. Kulesza, L. Häggman, G. Boschloo, A. Hagfeldt, Physicochemical identity and charge storage properties of battery-type nickel oxide material and its composites with activated carbon Narjes, Electrochim. Actamica Acta. 194 (2016) 480–488. doi:10.1016/j.electacta.2016.01.185.

[20]   X. Wang, M. Li, Z. Chang, Y. Wang, B. Chen, L. Zhang, Y. Wu, Orientated Co_3O_4 Nanocrystals on MWCNTs as Superior Battery-Type Positive Electrode Material for a Hybrid Capacitor, J. Electrochem. Soc. 162 (2015) A1966–A1971. doi:10.1149/2.0041511jes.

[21]   Y. Chuminjak, S. Daothong, A. Kuntarug, D. Phokharatkul, M. Horprathum, A. Wisitsoraat, A. Tuantranont, J. Jakmunee, P. Singjai, High-performance Electrochemical Energy Storage Electrodes Based on Nickel Oxide-coated Nickel Foam Prepared by Sparking Method, Electrochim. Acta. 238 (2017) 298–309. doi:10.1016/j.electacta.2017.03.190.

[22]   H. Lai, Q. Wu, J. Zhao, L. Shang, H. Li, R. Che, Z. Lyu, J. Xiong, L. Yang, X. Wang, Z. Hu, Mesostructured NiO/Ni composites for high-performance electrochemical energy storage, Energy Environ. Sci. 9 (2016) 2053–2060. doi:10.1039/c6ee00603e.

[23]   G. Meng, Q. Yang, X. Wu, P. Wan, Y. Li, X. Lei, X. Sun, J. Liu, Hierarchical mesoporous NiO nanoarrays with ultrahigh capacitance for aqueous hybrid supercapacitor, Nano Energy. 30 (2016) 831–839. doi:10.1016/j.nanoen.2016.09.012.

[24]   J. Lin, Y. Liu, Y. Wang, H. Jia, S. Chen, J. Qi, C. Qu, J. Cao, W. Fei, J. Feng, Designed formation of $NiO@C@Cu_2O$ hybrid arrays as battery-like electrode with enhanced electrochemical performances, Ceram. Int. 43 (2017) 15410–15417. doi:10.1016/j.ceramint.2017.08.082.

[25]   Y. Gogotsi, R.M. Penner, Energy Storage in Nanomaterials - Capacitive, Pseudocapacitive, or Battery-like?, ACS Nano. 12 (2018) 2081–2083. doi:10.1021/acsnano.8b01914.

[26]   Y. Ruan, C. Wang, J. Jiang, Nanostructured Ni compounds as electrode materials towards high-performance electrochemical capacitors, J. Mater. Chem. A. 4 (2016) 14509–14538. doi:10.1039/c6ta05104a.

[27]   Y. Wang, C.X. Guo, J. Liu, T. Chen, H. Yang, C.M. Li, CeO_2 nanoparticles/graphene nanocomposite-based high performance supercapacitor, Dalt. Trans. 40 (2011) 6388. doi:10.1039/c1dt10397k.

[28]   A.S. Dezfuli, M.R. Ganjali, H.R. Naderi, P. Norouzi, A high performance supercapacitor based on a ceria/graphene nanocomposite synthesized by a facile sonochemical method, RSC Adv. 5 (2015) 46050–46058. doi:10.1039/C5RA02957K.

[29]   S. Maiti, A. Pramanik, S. Mahanty, Extraordinarily high pseudocapacitance of metal organic framework derived nanostructured cerium oxide, Chem. Commun. 50 (2014) 11717–11720. doi:10.1039/C4CC05363J.

[30]   W. Shan, M. Luo, P. Ying, W. Shen, C. Li, Reduction property and catalytic activity of $Ce_{1-X}Ni_XO_2$ mixed oxide catalysts for CH_4 oxidation, Appl. Catal. A. 246 (2003) 1–9. doi:10.1016/S0926-860X(02)00659-2.

[31]   G. Wrobel, M.P. Sohier, A. D'Huysser, J.P. Bonnelle, J.P. Marcq, Hydrogenation catalysts based on nickel and rare earth oxides. Part II: XRD, electron microscopy and XPS studies of the cerium-nickel-oxygen-hydrogen system, Appl. Catal. A Gen. 101 (1993) 73–93. doi:10.1016/0926-860X(93)80139-H.

[32]   S. Mahammadunnisa, P. Manoj Kumar Reddy, N. Lingaiah, C. Subrahmanyam, $NiO/Ce_{1-x}Ni_xO_{2-\delta}$ as an alternative to noble metal catalysts for CO oxidation, Catal. Sci. Technol. 3 (2013) 730–736. doi:10.1039/c2cy20641b.

[33] M. Nolan, Enhanced oxygen vacancy formation in ceria (111) and (110) surfaces doped with divalent cations, J. Mater. Chem. 21 (2011) 9160–9168. doi:10.1039/c1jm11238d.

[34] D. Tian, C. Zeng, Y. Fu, H. Wang, H. Luo, C. Xiang, Y. Wei, K. Li, X. Zhu, A DFT study of the structural, electronic and optical properties of transition metal doped fluorite oxides: $Ce_{0.75}M_{0.25}O_2$ (M=Fe, Co, Ni), Solid State Commun. 231–232 (2016) 68–79. doi:10.1016/j.ssc.2016.01.011.

[35] Z. Ji, X. Shen, H. Zhou, K. Chen, Facile synthesis of reduced graphene oxide/CeO_2 nanocomposites and their application in supercapacitors, Ceram. Int. 41 (2015) 8710–8716. doi:10.1016/j.ceramint.2015.03.089.

[36] X. Zhang, W. Shi, J. Zhu, W. Zhao, J. Ma, S. Mhaisalkar, T.L. Maria, Y. Yang, H. Zhang, H.H. Hng, Q. Yan, Synthesis of porous NiO nanocrystals with controllable surface area and their application as supercapacitor electrodes, Nano Res. 3 (2010) 643–652. doi:10.1007/s12274-010-0024-6.

[37] C. Wang, D. Wang, Q. Wang, H. Chen, Fabrication and lithium storage performance of three-dimensional porous NiO as anode for lithium-ion battery, J. Power Sources. 195 (2010) 7432–7437. doi:10.1016/j.jpowsour.2010.04.090.

[38] N. Padmanathan, S. Selladurai, Electrochemical capacitance of porous $NiO-CeO_2$ binary oxide synthesized via sol-gel technique for supercapacitor, Ionics (Kiel). 20 (2014) 409–420. doi:10.1007/s11581-013-0989-8.

[39] B. Cela, D.A. De MacEdo, G.L. De Souza, A.E. Martinelli, R.M. Do Nascimento, C.A. Paskocimas, NiO-CGO in situ nanocomposite attainment: One step synthesis, J. Power Sources. 196 (2011) 2539–2544. doi:10.1016/j.jpowsour.2010.11.026.

[40] J.P.F. Grilo, C.G. Moura, D.A. Macedo, S. Rajesh, F.M.L. Figueiredo, F.M.B. Marques, R.M. Nascimento, Effect of composition on the structural development and electrical conductivity of NiO-GDC composites obtained by one-step synthesis, Ceram. Int. (2017) 0–1. doi:10.1016/j.ceramint.2017.04.027.

[41] J.P.F. Grilo, D.A. Macedo, R.M. Nascimento, F.M.B. Marques, Assessment of NiO-CGO composites as cermet precursors, Solid State Ionics. 321 (2018) 115–121. doi:10.1016/j.ssi.2018.04.014.

[42] D.A. Macedo, G.L. Souza, B. Cela, C.A. Paskocimas, A.E. Martinelli, F.M.L. Figueiredo, F.M.B. Marques, R.M. Nascimento, A versatile route for the preparation of Ni-CGO cermets from nanocomposite powders, Ceram. Int. 39 (2013) 4321–4328. doi:10.1016/j.ceramint.2012.11.014.

[43] D. Joung, V. Singh, S. Park, A. Schulte, S. Seal, S.I. Khondaker, Anchoring ceria nanoparticles on reduced graphene oxide and their electronic transport properties, J. Phys. Chem. C. 115 (2011) 24494–24500. doi:10.1021/jp206485v.

[44] T.H. de Keijser, J.I. Langford, E.J. Mittemeijer, A.B.P. Vogels, Use of the Voigt function in a single-line method for the analysis of X-ray diffraction line broadening, J. Appl. Crystallogr. 15 (1982) 308–314. doi:10.1107/S0021889882012035.

[45] J. Iqbal, A. Numan, S. Rafique, R. Jafer, S. Mohamad, K. Ramesh, S. Ramesh, High performance supercapattery incorporating ternary nanocomposite of multiwalled carbon nanotubes decorated with Co_3O_4 nanograins and silver nanoparticles as electrode material, Electrochim. Acta. 278 (2018) 72–82. doi:10.1016/j.electacta.2018.05.040.

[46] A.J.M. Araújo, J.P.F. Grilo, F.J.A. Loureiro, L.F.A. Campos, C.A. Paskocimas, R.M. Nascimento, D.A. Macedo, Designing experiments for the preparation of Ni-GDC cermets with controlled porosity as SOFC anode materials: effects on the electrical properties, Ceram. Int. (2018) 0–1. doi:10.1016/j.ceramint.2018.09.115.

[47] B. Solsona, P. Concepción, S. Hernández, B. Demicol, J.M.L. Nieto, Oxidative dehydrogenation of ethane over $NiO-CeO_2$ mixed oxides catalysts, Catal. Today. 180 (2012) 51–58. doi:10.1016/j.cattod.2011.03.056.

[48] T.H. Santos, J.P.F. Grilo, F.J.A. Loureiro, D.P. Fagg, F.C. Fonseca, D.A. Macedo, Structure,

densification and electrical properties of Gd^{3+} and Cu^{2+} co-doped ceria solid electrolytes for SOFC applications: Effects of Gd_2O_3 content, Ceram. Int. 44 (2018) 2745–2751. doi:10.1016/j.ceramint.2017.11.009.

[49] S. Anirban, T. Paul, A. Dutta, Vacancy mediated ionic conduction in Dy substituted nanoceria: a structure-property correlation study, RSC Adv. 5 (2015) 50186–50195. doi:10.1039/c5ra06730h.

[50] N.M. Deraz, Effect of NiO content on structural, surface and catalytic characteristics of nano-crystalline NiO/CeO_2 system, Ceram. Int. 38 (2012) 747–753. doi:10.1016/j.ceramint.2011.07.068.

[51] D. Srinivas, C.V.V. Satyanarayana, H.S. Potdar, P. Ratnasamy, Structural studies on NiO-CeO_2-ZrO_2 catalysts for steam reforming of ethanol, Appl. Catal. A Gen. 246 (2003) 323–334. doi:10.1016/S0926-860X(03)00085-1.

[52] J. Sørensen, O. T., & Rouquerol, Sample controlled thermal analysis: origin, goals, multiple forms, applications and future, Springer Science & Business Media, 2013. doi:10.1007/978-1-4757-3735-6.

[53] J. Stringer, The Importance of Short-Circuit and Related Transport Processes in High-Temperature Oxidation, in: M.S. Seltzer, R.I. Jaffee (Eds.), Defects Transp. Oxides, Springer US, Boston, MA, 1974: pp. 495–517. doi:10.1007/978-1-4615-8723-1_28.

[54] S. Kumar, Y.J. Kim, B.H. Koo, C.G. Lee, Structural and Magnetic Properties of Ni Doped CeO_2 Nanoparticles, J. Nanosci. Nanotechnol. 10 (2010) 7204–7207. doi:10.1166/jnn.2010.2751.

[55] W. Derafa, F. Paloukis, B. Mewafy, W. Baaziz, O. Ersen, C. Petit, G. Corbel, S. Zafeiratos, Synthesis and characterization of nickel-doped ceria nanoparticles with improved surface reducibility, RSC Adv. 8 (2018) 40712–40719. doi:10.1039/C8RA07995A.

[56] F.A. Kröger, The chemistry of imperfect crystals, North-Holand, Amsterdam, 1964.

[57] X. Wang, M. Shen, J. Wang, S. Fabris, Enhanced oxygen buffering by substitutional and interstitial Ni point defects in ceria: A first-principles DFT+U study, J. Phys. Chem. C. 114 (2010) 10221–10228. doi:10.1021/jp101100f.

[58] K.I. Maslakov, Y.A. Teterin, A.J. Popel, A.Y. Teterin, K.E. Ivanov, S.N. Kalmykov, V.G. Petrov, P.K. Petrov, I. Farnan, XPS study of ion irradiated and unirradiated CeO_2 bulk and thin film samples, Appl. Surf. Sci. 448 (2018) 154–162. doi:10.1016/j.apsusc.2018.04.077.

[59] S. Phokha, S. Hunpratub, B. Usher, A. Pimsawat, N. Chanlek, S. Maensiri, Effects of CeO_2 nanoparticles on electrochemical properties of carbon/CeO_2 composites, Appl. Surf. Sci. 446 (2018) 36–46. doi:10.1016/j.apsusc.2018.02.209.

[60] P.V.R. Rao, V.P. Kumar, G.S. Rao, K.V.R. Chary, Vapor phase selective hydrogenation of acetone to methyl isobutyl ketone (MIBK) over Ni/CeO_2 catalysts, Catal. Sci. Technol. 2 (2012) 1665–1673. doi:10.1039/c2cy20021j.

[61] K. Hauffe, Oxidation of metals, 1965.

[62] S. Phokha, S. Hunpratub, N. Chanlek, S. Sonsupap, S. Maensiri, Synthesis, characterization and electrochemical performance of carbon/Ni-doped CeO_2 composites, J. Alloys Compd. 750 (2018) 788–797. doi:10.1016/j.jallcom.2018.04.053.

[63] S. Ci, Z. Wen, Y. Qian, S. Mao, S. Cui, J. Chen, NiO-Microflower Formed by Nanowire-weaving Nanosheets with Interconnected Ni-network Decoration as Supercapacitor Electrode, Sci. Rep. 5 (2015) 11919. doi:10.1038/srep11919.

[64] A. Allagui, A.H. Alami, E.A. Baranova, R. Wüthrich, Size-dependent capacitance of NiO nanoparticles synthesized with cathodic contact glow discharge electrolysis, J. Power Sources. 262 (2014) 178–182. doi:10.1016/j.jpowsour.2014.03.104.

[65] K. Wang, X. Shi, Z. Zhang, X. Ma, Y. Lu, H. Wang, Size-dependent capacitance of NiO nanoparticles synthesized from Ni-based coordination polymer precursors with different crystallinity, J. Alloys Compd. 632 (2015) 361–367. doi:10.1016/j.jallcom.2015.01.252.

[66] M. Kumar, J. Yun, V. Bhatt, B. Singh, J. Kim, J. Kim, B. Soo, C. Yeon, Electrochimica Acta

Role of Ce^{3+} valence state and surface oxygen vacancies on enhanced electrochemical performance of single step solvothermally synthesized CeO_2 nanoparticles, Electrochim. Acta. 284 (2018) 709–720. doi:10.1016/j.electacta.2018.07.184.

[67] M. Forghani, S.W. Donne, Method Comparison for Deconvoluting Capacitive and Pseudo-Capacitive Contributions to Electrochemical Capacitor Electrode Behavior, J. Electrochem. Soc. 165 (2018) A664–A673. doi:10.1149/2.0931803jes.

[68] K.-J. Huang, J.-Z. Zhang, J.-L. Cai, Preparation of porous layered molybdenum selenide-graphene composites on Ni foam for high-performance supercapacitor and electrochemical sensing, Electrochim. Acta. 180 (2015) 770–777. doi:10.1016/j.electacta.2015.09.016.

[69] M. Tahir, L. Pan, F. Idrees, X. Zhang, L. Wang, J.J. Zou, Z.L. Wang, Electrocatalytic oxygen evolution reaction for energy conversion and storage: A comprehensive review, Nano Energy. 37 (2017) 136–157. doi:10.1016/j.nanoen.2017.05.022.

[70] L. Lu, Y. Xie, Z. Zhao, Improved electrochemical stability of $Ni_xCo_{2x}(OH)_{6x}/NiCo_2O_4$ electrode material, J. Alloys Compd. 731 (2018) 903–913. doi:10.1016/j.jallcom.2017.10.119.

[71] S.A. Pawar, D.S. Patil, J.C. Shin, Electrochemical battery-type supercapacitor based on chemosynthesized Cu_2S-Ag_2S composite electrode, Electrochim. Acta. 259 (2018) 664–675. doi:10.1016/j.electacta.2017.11.006.

[72] X. Lang, H. Zhang, X. Xue, C. Li, X. Sun, Z. Liu, H. Nan, X. Hu, H. Tian, Rational design of $La_{0.85}Sr_{0.15}MnO_3@NiCo_2O_4$ Core–Shell architecture supported on Ni foam for high performance supercapacitors, J. Power Sources. 402 (2018) 213–220. doi:10.1016/j.jpowsour.2018.09.040.

[73] Z. Li, W. Zhang, H. Wang, B. Yang, Two-dimensional perovskite $LaNiO_3$ nanosheets with hierarchical porous structure for high-rate capacitive energy storage, Electrochim. Acta. 258 (2017) 561–570. doi:10.1016/j.electacta.2017.11.099.

Table caption

Table 1. Quantitative phase analysis (wt.%), lattice parameter (a) and crystallite size (D_{XRD}) estimated by Rietveld refinement of the XRD data.
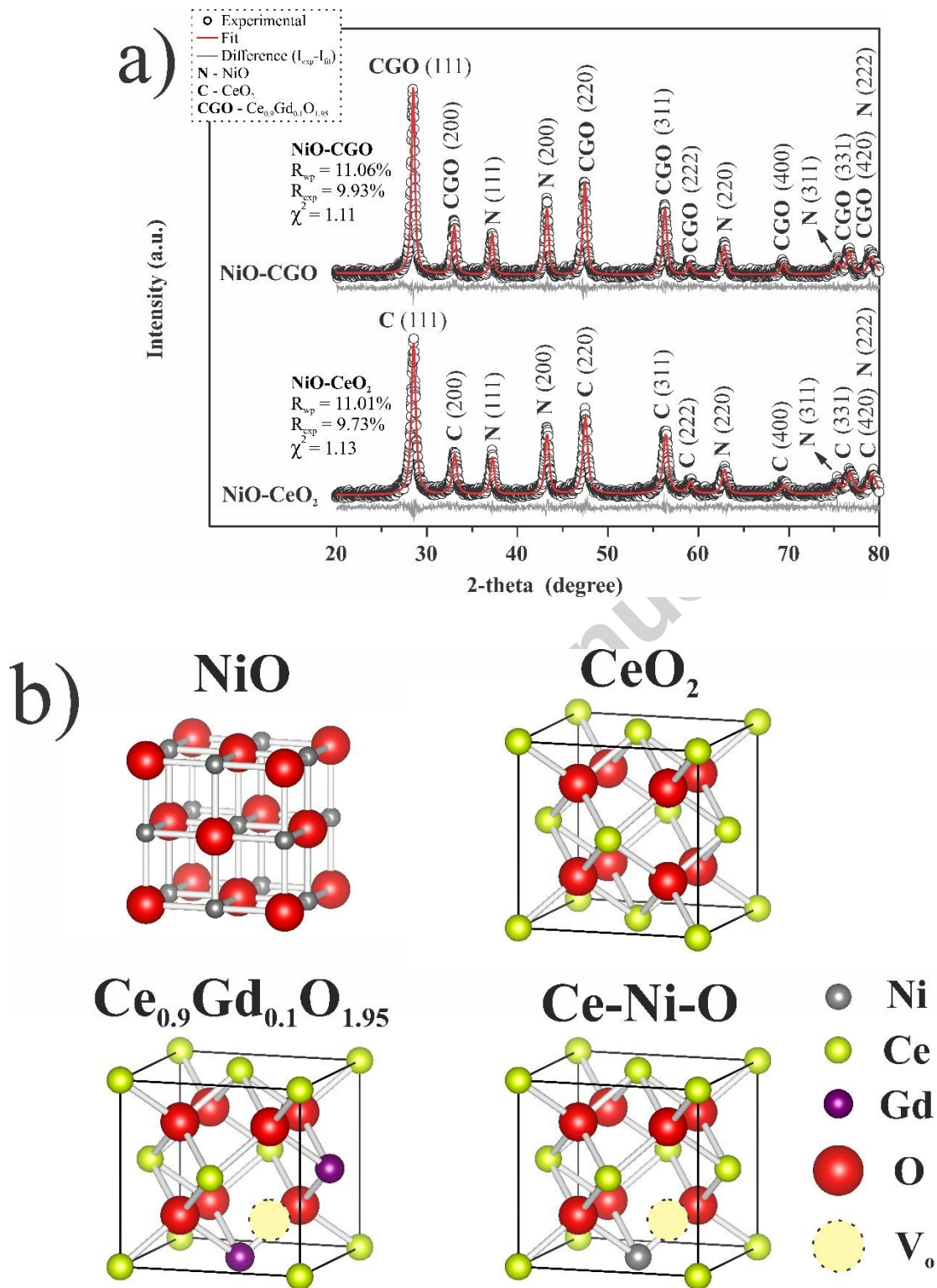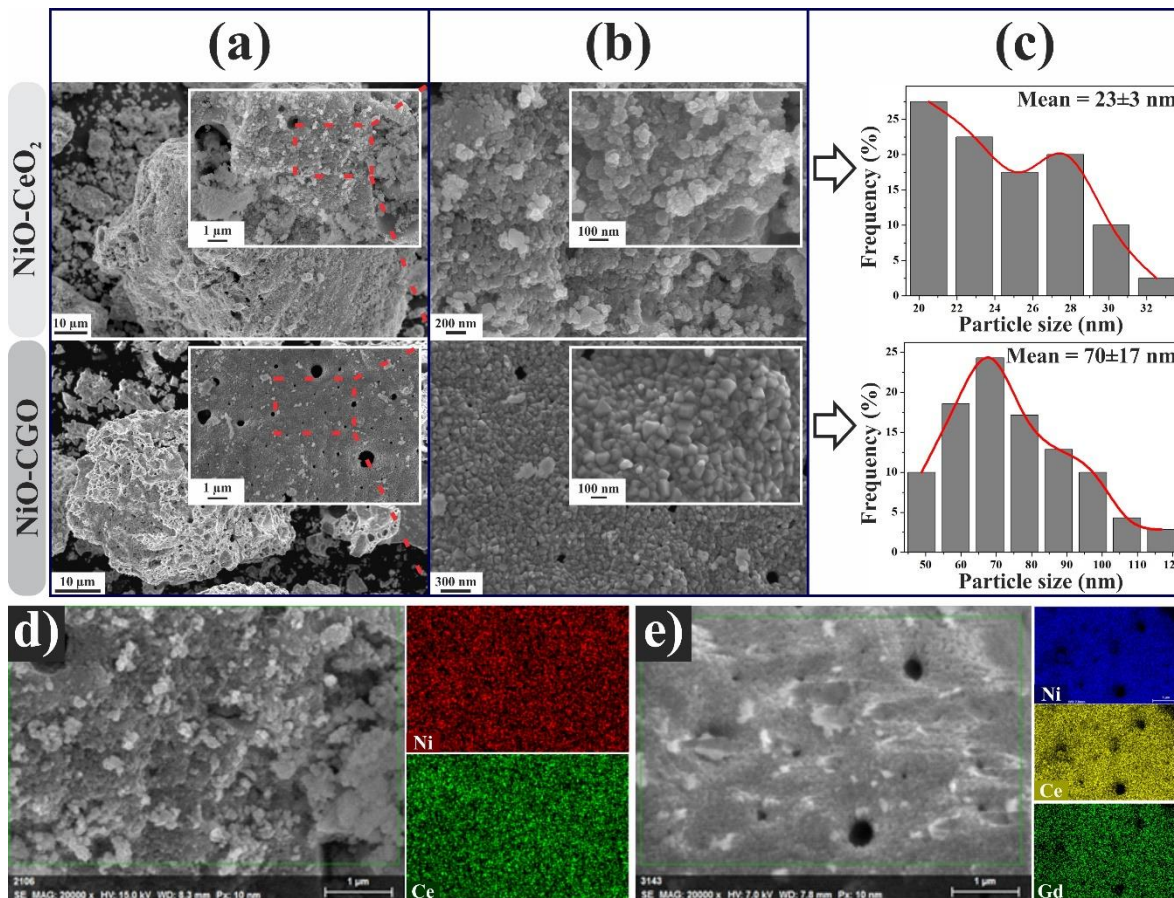
Figure caption

Fig. 1. Co-precipitation method scheme used to obtain the composite powders.

Fig. 2. (a) Rietveld refinement XRD patterns of calcined powders and (b) crystal structures of the obtained phases.

Fig. 3. FESEM images with (a) low and (b) high-magnification of calcined powders, (c) their corresponding particle size distributions and EDS mapping of (d) NiO-CeO$_2$ and (e) NiO-CGO powders.
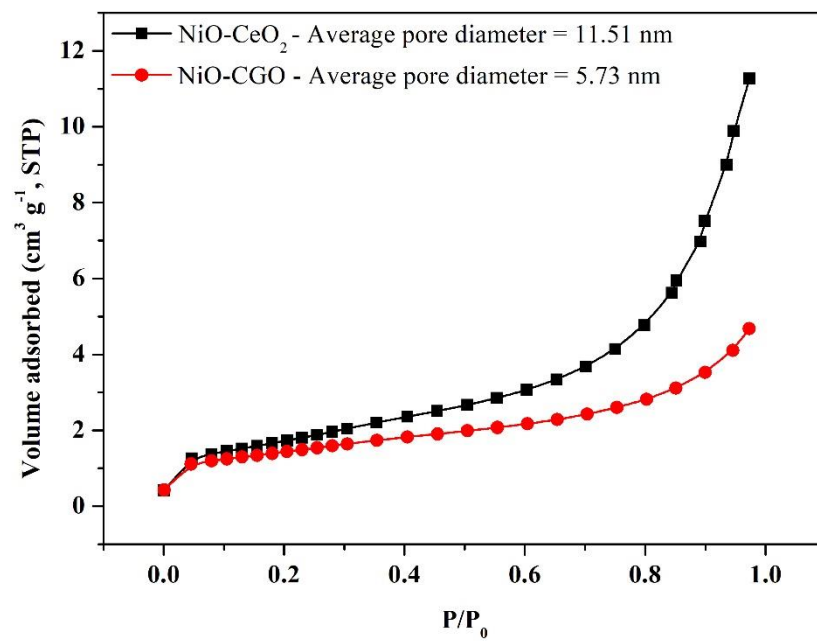
Fig. 4. N$_2$ adsorption isotherms of NiO-CeO$_2$ and NiO-CGO powders.

Fig. 5. High-resolution XPS spectra of NiO-CeO$_2$ and NiO-CGO powders: (a) Overview, (b) Ce 3d/ Ni 2p and (c) O 1s.

Fig. 6. CV curves of electrodes made of (a) NiO-CeO$_2$ and (b) NiO-CGO powders, measured at different scan rates in 3 M KOH. (c) Comparison of CV curves recorded at 100 mV s^{-1}. (d) Plots of i$_p$ versus v$^{1/2}$ used to calculate the slopes for the anodic and cathodic scans, with scan rates varied from 0.5 to 100 mV s^{-1}. (e) Specific capacities obtained from CV tests at different scan rates.

Fig. 7. GCD curve of the NiO-CeO$_2$ electrode at 0.5 A g^{-1}.

Fig. 8. Nyquist plots of the NiO-CeO$_2$ and NiO-CGO electrodes in 3 M KOH electrolyte with the inset showing the high-frequency region.

Table 1. Quantitative phase analysis (wt.%), lattice parameter (a) and crystallite size (D_{XRD}) estimated by Rietveld refinement of the XRD data.

Sample	wt.%		a (Å)		D_{XRD} (nm)	
	NiO	Ceria phase	NiO	Ceria phase	NiO	Ceria phase
NiO-CeO$_2$	49.00	51.00	4.179	5.410	25	21
NiO-CGO	48.80	51.20	4.180	5.418	36	28

Fig. 1. Co-precipitation method scheme used to obtain the composite powders.

Fig. 2. (a) Rietveld refinement XRD patterns of calcined powders and (b) crystal structures of the obtained phases.

Fig. 3. FESEM images with (a) low and (b) high-magnification of calcined powders, (c) their corresponding particle size distributions and EDS mapping of (d) NiO-CeO$_2$ and (e) NiO-CGO powders.
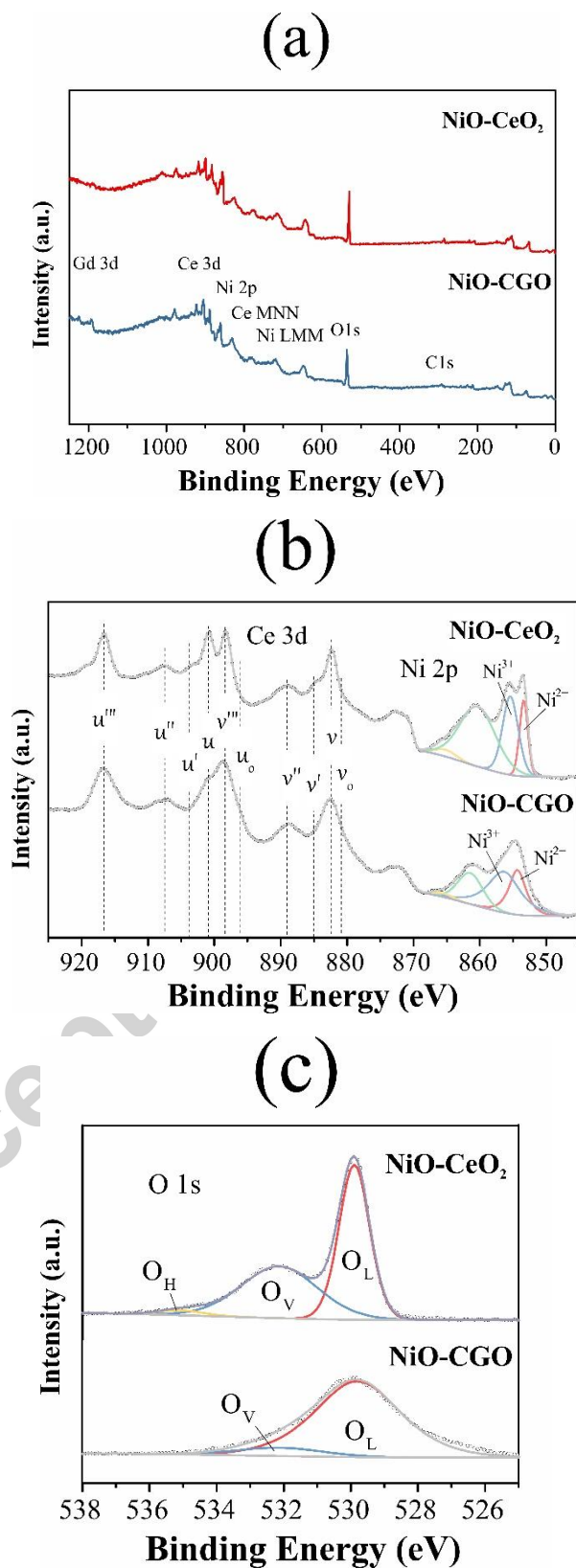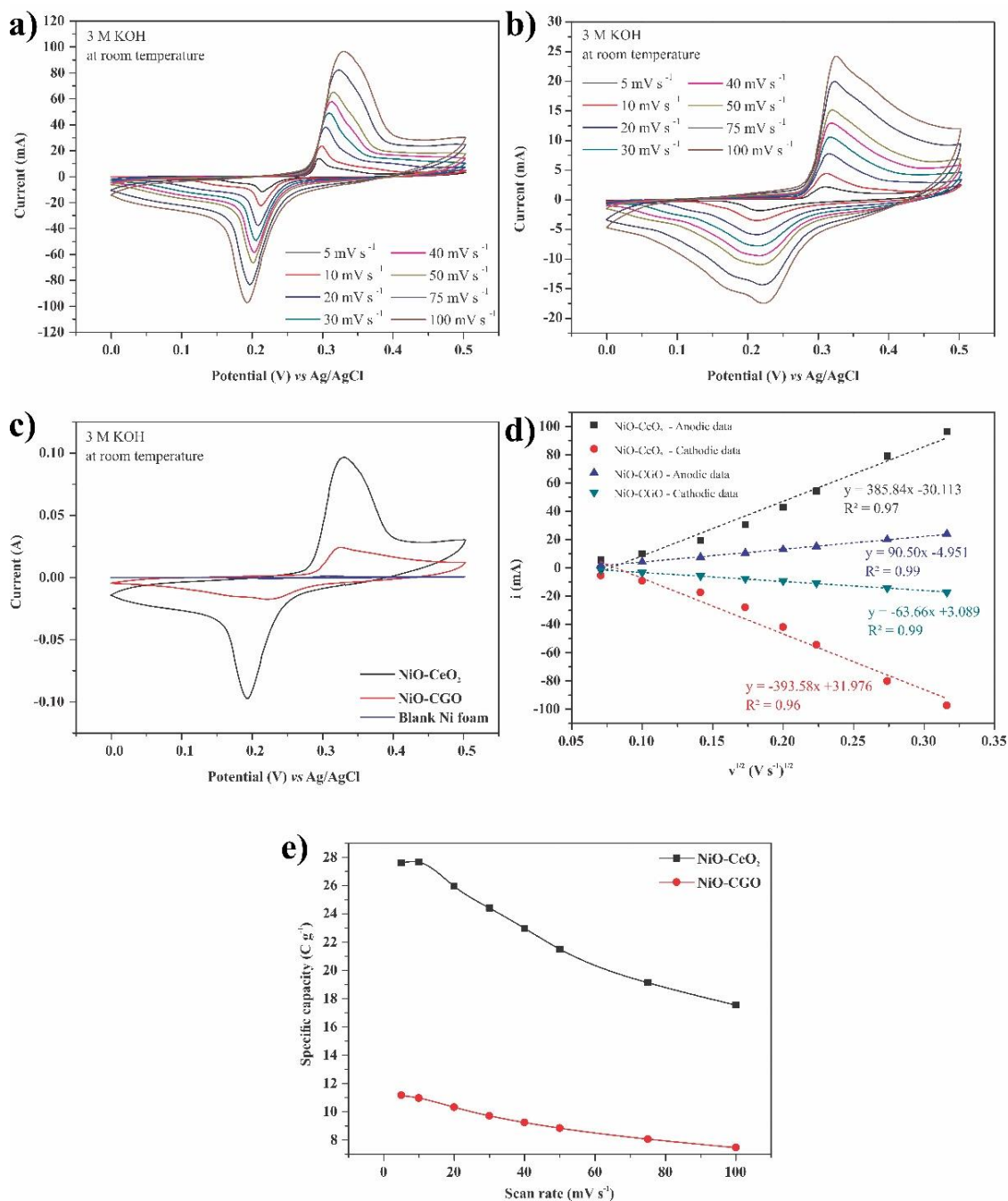
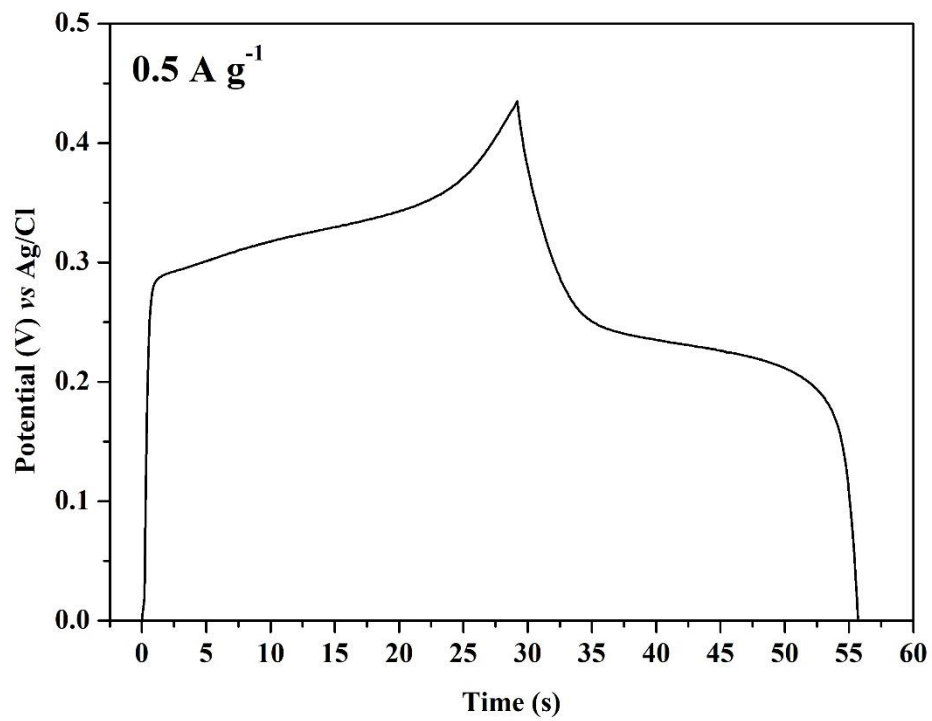**Fig. 4.** N_2 adsorption isotherms of NiO-CeO$_2$ and NiO-CGO powders.

Fig. 5. High-resolution XPS spectra of NiO-CeO$_2$ and NiO-CGO powders: (a) Overview, (b) Ce 3d/ Ni 2p and (c) O 1s.
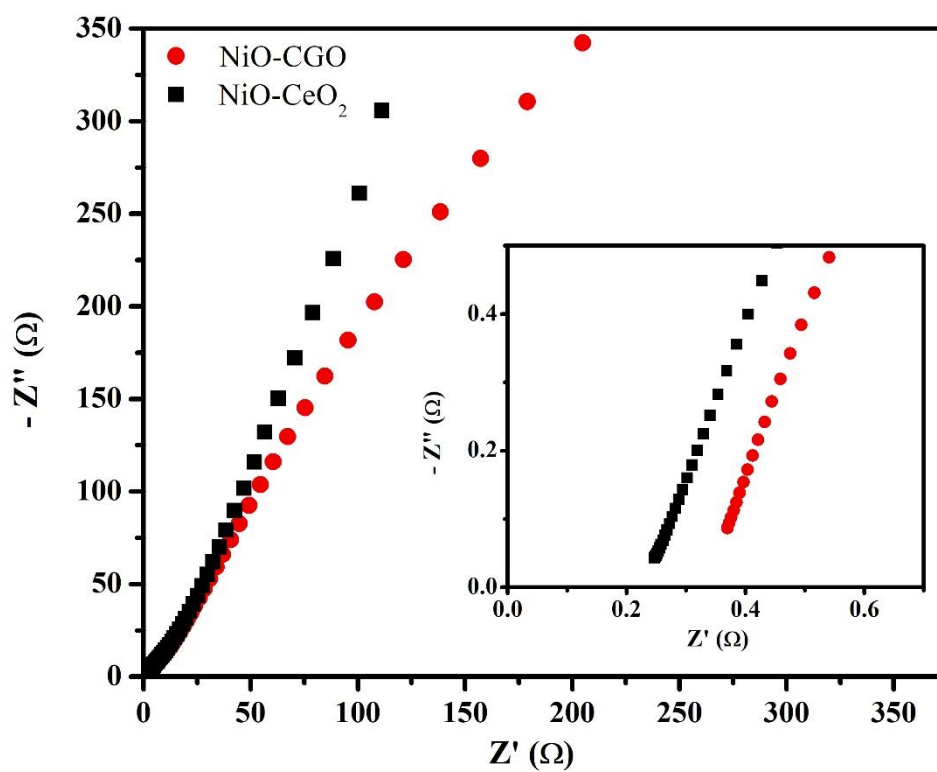
Fig. 6. CV curves of electrodes made of (a) NiO-CeO$_2$ and (b) NiO-CGO powders, measured at different scan rates in 3 M KOH. (c) Comparison of CV curves recorded at 100 mV s^{-1}. (d) Plots of i$_p$ versus v$^{1/2}$ used to calculate the slopes for the anodic and cathodic scans, with scan rates varied from 0.5 to 100 mV s^{-1}. (e) Specific capacities obtained from CV tests at different scan rates.

Fig. 7. GCD curve of the NiO-CeO$_2$ electrode at 0.5 A g^{-1}.

Fig. 8. Nyquist plots of the NiO-CeO$_2$ and NiO-CGO electrodes in 3 M KOH electrolyte with the inset showing the high-frequency region.

Highlights

- Ni-ceria based systems as battery-like materials;

- (Ni or Gd)-doping effect on the performance of ceria in alkaline (3 M KOH) solution;

- NiO + Ce-Ni-O solid solution with better battery-like behavior than NiO-Ce$_{0.9}$Gd$_{0.1}$O$_{1.95}$.

- Battery-like behavior enhanced by surface defects.